Electronic Supplementary Material (ESI)

Evaluation of Microflow Configurations for Scale Inhibition and Serial X-ray Diffraction Analysis of Crystallization Processes

Mark A. Levenstein,[1, 2†] Yi-Yeoun Kim,[2] Liam Hunter,[2] Clara Anduix-Canto,[2‡] Carlos González Niño,[1] Sarah J. Day,[3] Shunbo Li,[2§] William J. Marchant,[2] Phillip A. Lee,[2] Chiu C. Tang,[3] Manfred Burghammer,[4] Fiona C. Meldrum*[2] and Nikil Kapur*[1]

[1] School of Mechanical Engineering, University of Leeds, Woodhouse Lane, Leeds LS2 9JT, United Kingdom, *Email: N.Kapur@leeds.ac.uk*

[2] School of Chemistry, University of Leeds, Woodhouse Lane, Leeds LS2 9JT, United Kingdom, *Email: F.Meldrum@leeds.ac.uk*

[3] Diamond Light Source, Didcot OX11 0DE, United Kingdom

[4] European Synchrotron Radiation Facility, F-38043 Grenoble, France

† Present address: Department of Mechanical Science and Engineering, University of Illinois at Urbana-Champaign, 1206 W Green Street, Urbana, IL, 61801, USA

‡ Present address: Alba Synchrotron Light Source, Carrer de la Llum 2-26, 08290 Cerdanyola del Vallès, Barcelona, Spain

§ Present address: School of Optoelectronic Engineering, Chongqing University, Chongqing 400044, China

Summary of Matlab Script for Automated X-ray Data Processing:

A Matlab algorithm was developed to cycle through a multi-frame exposure from ESRF ID13, where frames containing oil scattering are discarded and frames containing water scattering are background subtracted. The background subtraction routine consists of subtracting a frame from the same exposure – but one not containing any crystals – from the target frames. Then stray pixels, consisting of residual scattering noise, are removed with a threshold identified for each experiment (typically 20-30 a.u.). These frames are summed together to form a composite 2D pattern incorporating all the diffraction observed during that exposure. This pattern is then integrated and the detector parameters (pixel size, aspect ratio) and the sample-to-detector distance are taken into account to produce a 1D pattern displaying intensity as a function of 2θ. Reference data for particular crystal polymorphs are then plotted against these 1D patterns to identify particular peaks, where errors in peak position are typically $< 0.05°$.

A similar method is used to process single diffraction patterns obtained from 60-120s exposures at Diamond I11. In this case, a single pattern is background subtracted using a pattern of the same exposure length taken from the same channel or another channel from the same experiment before crystal growth was observed. For both ID13 and I11 data, it is not possible to use a single background reference for all channels for all experiments as small differences in sample-to-detector distance, texturing/imperfections in the Kapton windows, and possible beam clipping of channel walls, make each exposure too unique for application of a universal background reference. After background subtraction, a similar thresholding step is used in conjunction with a median filter (medfilt2) to remove noise. This is due to the higher noise observed at I11 compared to ID13, which is attributed to longer scan times, less suitable background references, lower performance of CCD vs. hybrid photon counting detectors, and a larger beam size/ irradiated volume. Finally, these processed patterns are integrated and compared with reference data. A copy of Matlab scripts for processing both single and multi-frame diffraction patterns can be found at https://doi.org/10.5518/755.

Table S1: Saturation Index (SI) and solution conditions utilised in continuous flow experiments at 4 mM final $CaCl_2$ and Na_2CO_3 concentration.

Condition	Polymorph	SI (*log IAP/K_s*)	pH	Ionic Strength (M)
23 °C	Calcite	2.536	10.683	0.0157
	Aragonite	2.391		
	Vaterite	1.964		
	ACC	0.446		
33 °C	Calcite	2.524	10.457	0.0153
	Aragonite	2.386		
	Vaterite	1.979		
	ACC	0.489		
38 °C	Calcite	2.516	10.347	0.0151
	Aragonite	2.381		
	Vaterite	1.982		
	ACC	0.511		
49 °C	Calcite	2.492	10.116	0.0145
	Aragonite	2.364		
	Vaterite	1.984		
	ACC	0.561		

IAP, pH and ionic strength values were calculated using Visual Minteq (KTH). K_s values for calcite, aragonite and vaterite were calculated from ref. 49 and the K_s value for ACC was calculated from ref. 50.

Table S2: Saturation Index (SI) and solution conditions utilised in segmented flow experiments.

Condition	Polymorph	SI (*log IAP/K_s*)	pH	Ionic Strength (M)
12.5 mM Ca^{2+} / 50 mM CO_3^{2-}	Calcite	3.287	11.161	0.1153
	Aragonite	3.142		
	Vaterite	2.715		
	ACC	1.197		
50 mM Ca^{2+} / 50 mM CO_3^{2-}	Calcite	3.777	10.969	0.1546
	Aragonite	3.632		
	Vaterite	3.205		
	ACC	1.687		

IAP, pH and ionic strength values were calculated using Visual Minteq (KTH). K_s values for calcite, aragonite and vaterite were calculated from ref. 49 and the K_s value for ACC was calculated from ref. 50.

Table S3: X-ray Beam Characteristics

	Energy (keV)	Beam Size (H x V μm^2)	Flux at sample (ph/s/0.1%BW)	Flux Density (ph/s/0.1%BW/μm^2)
Diamond I11	15	~200 x 200*	~7.1 x 10^{11}‡	1.8 x 10^{7}
ESRF ID13	13	15 x 12†	~1.5 x 10^{12}‡	8.3 x 10^{9}

***** obtained by reducing the normal beam size with slits

† obtained by defocusing from the regular focused beam size of 3x2 (HxV μm^2)

‡ flux values are approximate and may not represent current beamline performance

Table S4: X-ray Detector Specifications and Experimental Parameters

	Detector	Pixel Size (μm)	Pixel Aspect Ratio (H x V)	Maximum Frame Rate (Hz)	Sample-to-Detector Distance (mm)
Diamond I11	Pixium RF4343	148	2880 x 2881	~1-5*	~260
ESRF ID13	EigerX 4M	75	2070 x 2167	750	~115

***** dependent on the operational mode defining the active pixel range, i.e. pixel binning, and read-out time between frames

Fig. S1: DMC-XRD experimental setup at ESRF beamline ID13 showing the expanding window at the back of the device.

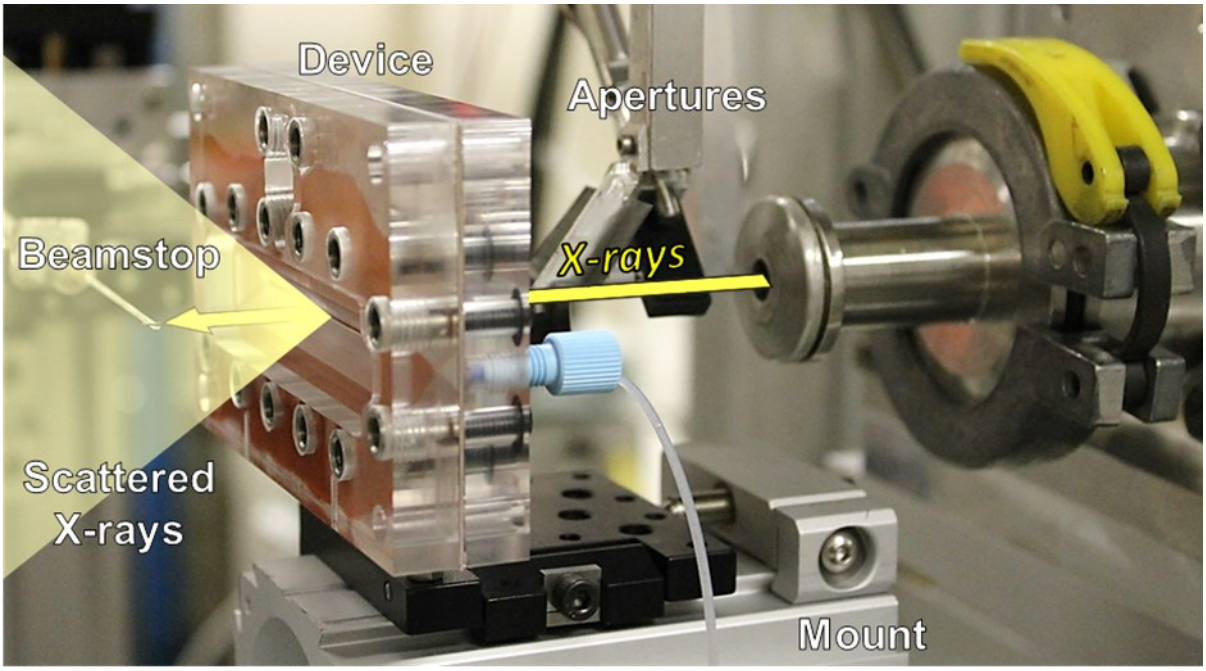

Fig. S2: High-resolution SEM micrograph of ground 58S porous bioactive glass.

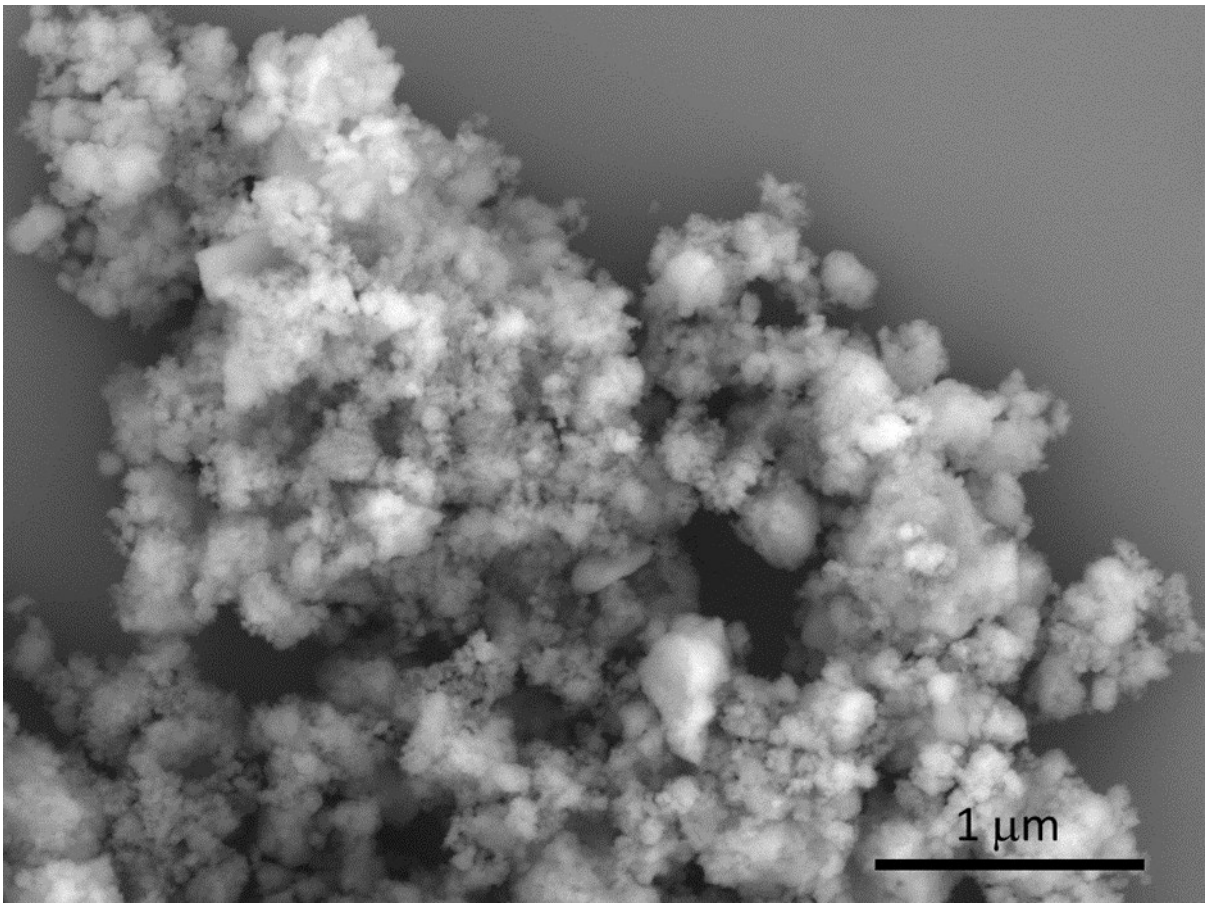

Fig. S3: The experimental set-up at Diamond beamline I11. The third inlet is shown to be connected to tubing for oil introduction. However, this inlet was plugged during continuous flow experiments.

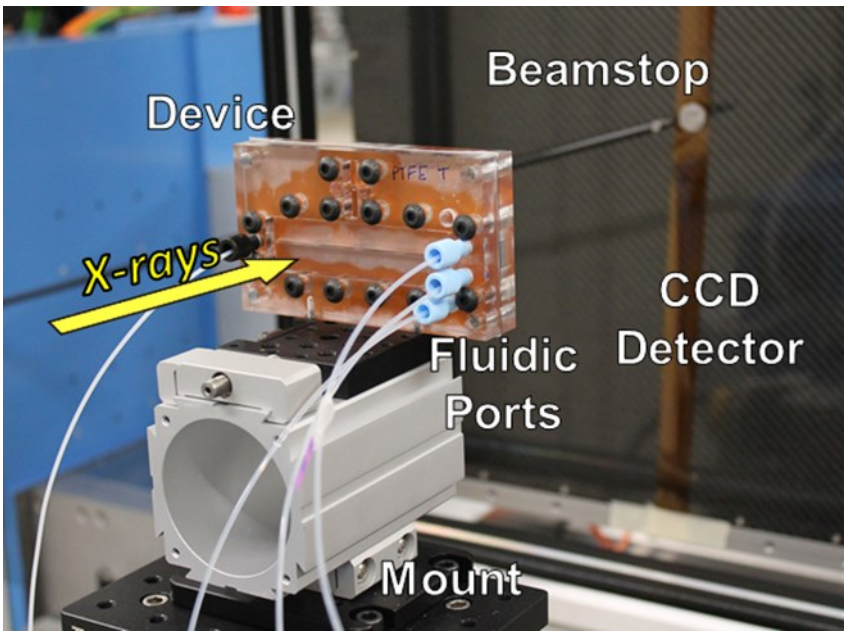

Fig. S4: Two-dimensional X-ray diffraction patterns from 60 s exposures at Diamond I11 revealing the scattering appearance of various device components.

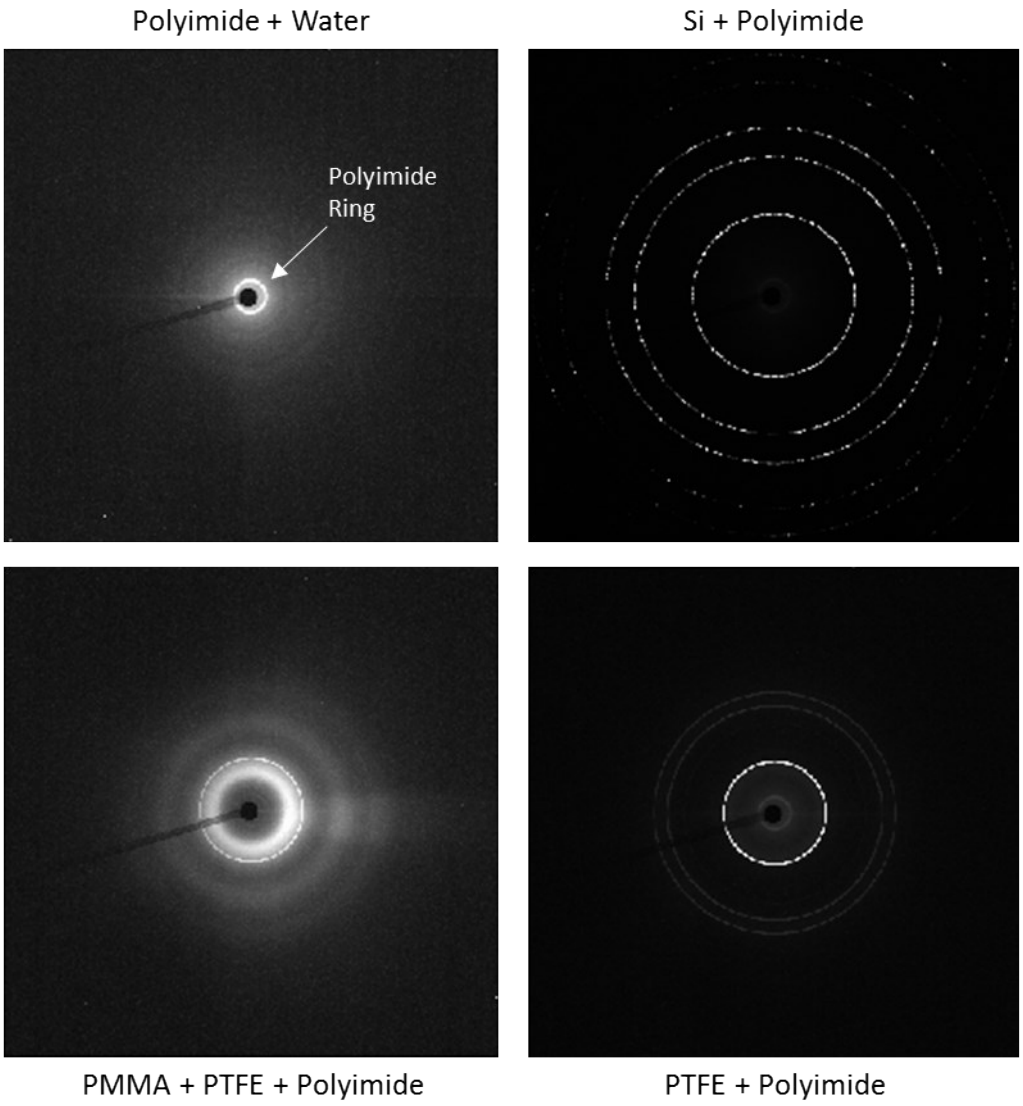

Fig. S5: (a) Mixing of two dye-containing solutions in the device. At the T-junction, a yellow dyed fluid meets a blue dyed fluid, and due to the low Reynolds number, a well-defined interface between them is maintained. However, by the time the flow reaches Position 1, the fluids have been mixed by diffusion and now appear green. (b) A corresponding Comsol Multiphysics® simulation of Ca^{2+} and CO^{2-} ions mixing in the device. Red fluid segments have a Ca^{2+} ion concentration of 8 mM, blue fluid segments contain no Ca^{2+} ions, and well-mixed green areas have a Ca^{2+} ion concentration of ~4 mM. (c) Plots of Ca^{2+} ion concentration along the x-direction at the y-centre of the channel for the indicated coloured lines on the diagram. The zero point for position on the graph is at the xy centre of the channel.

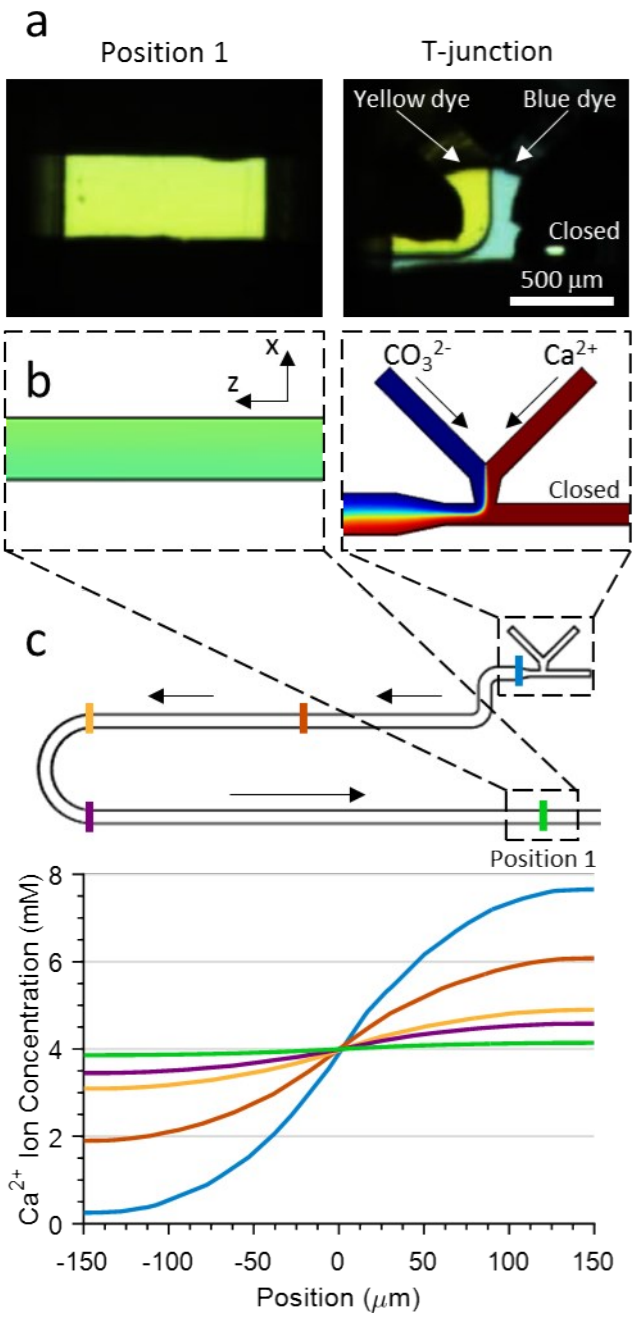

Fig. S6: High magnification SEM micrographs of (a) the T-junction, (b) Position 1, and (c) Position 2 after a continuous flow ambient temperature experiment.

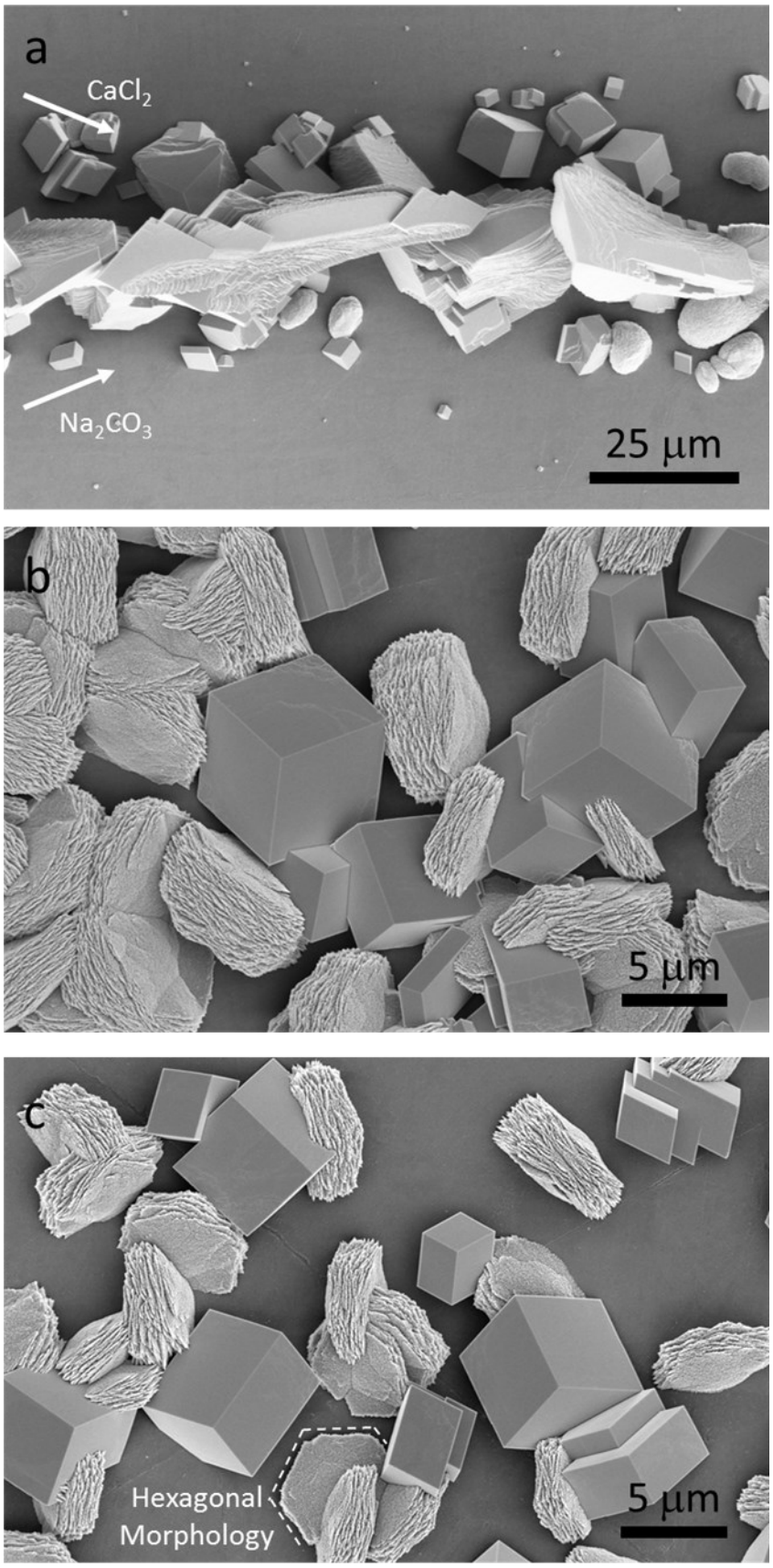

Fig. S7: (a-l) Optical micrographs taken from the ambient temperature continuous flow experiment at the indicated time and position. (m-o) Scanning electron micrographs of the bottom Kapton window revealing surface growth after running the experiment for 40 min. Scale bars are 100 μm in optical images and are 50 μm in SEM images.

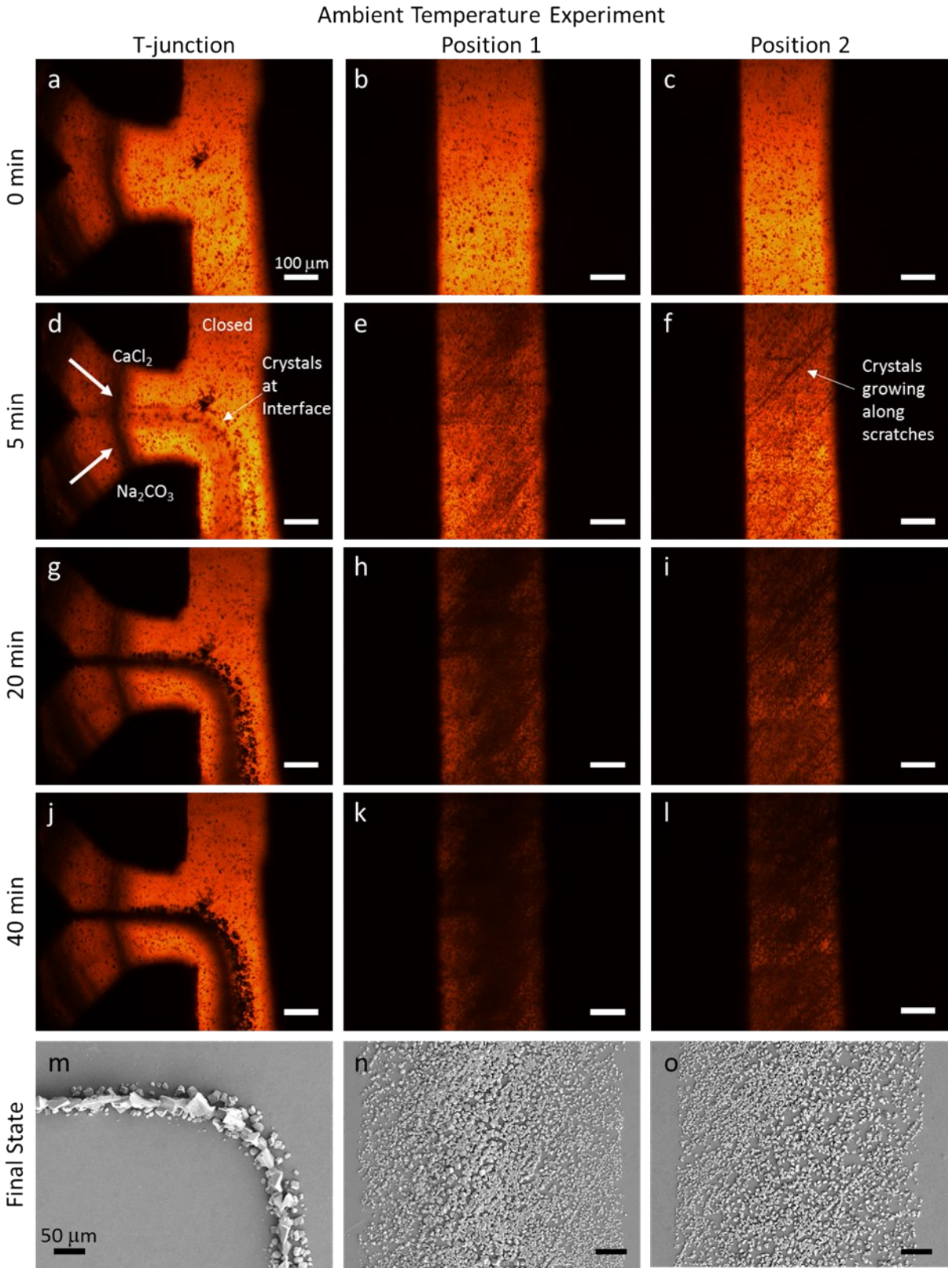

Fig. S8: Time-resolved diffraction patterns from the indicated channel position taken from the (a-c) ambient temperature and (d-f) temperature gradient continuous flow experiments.

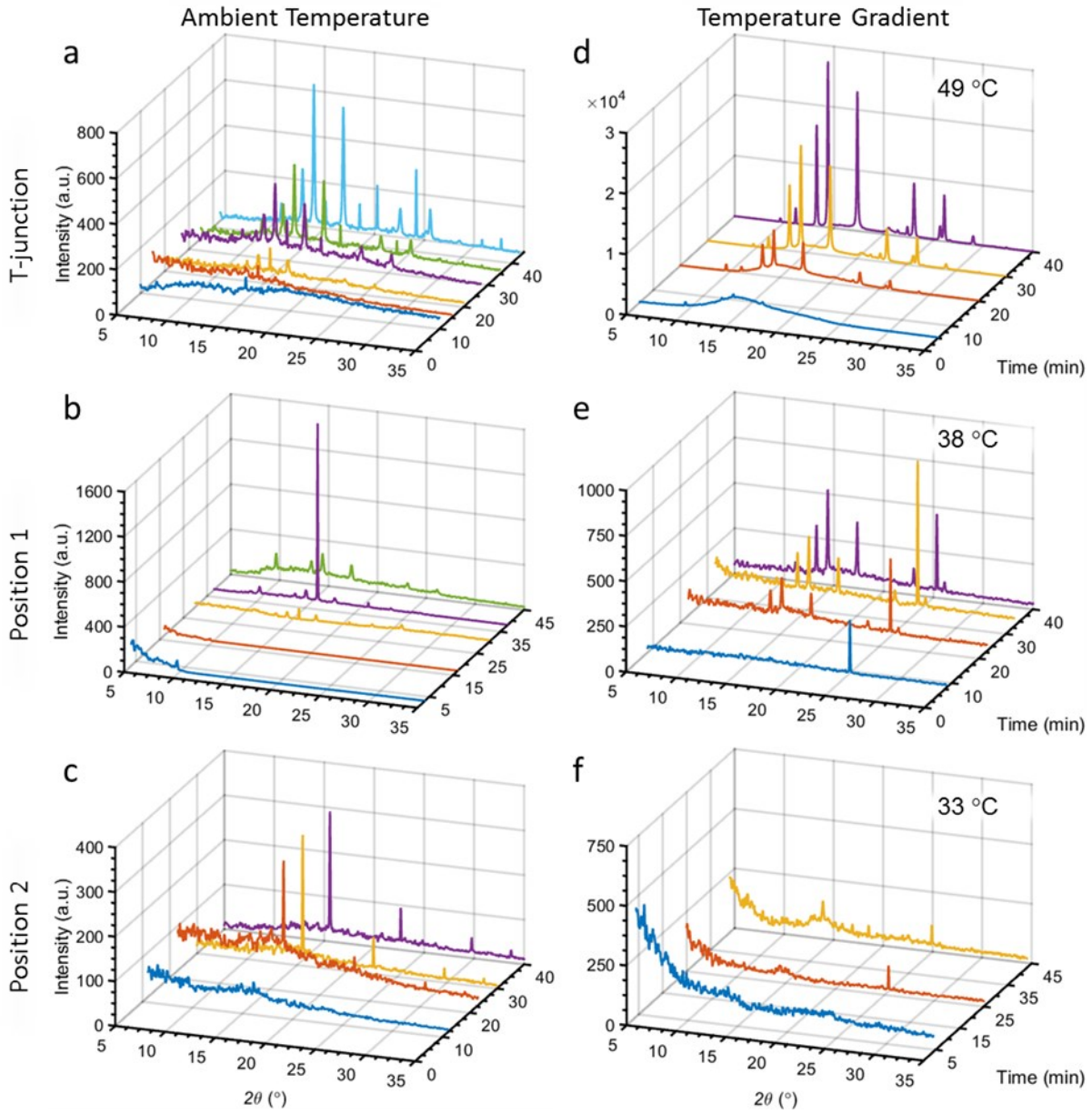

Fig. S9: Indexed final diffraction patterns from Figure S8 from the indicated channel positions: (a-c) ambient temperature and (d-f) temperature gradient experiments.

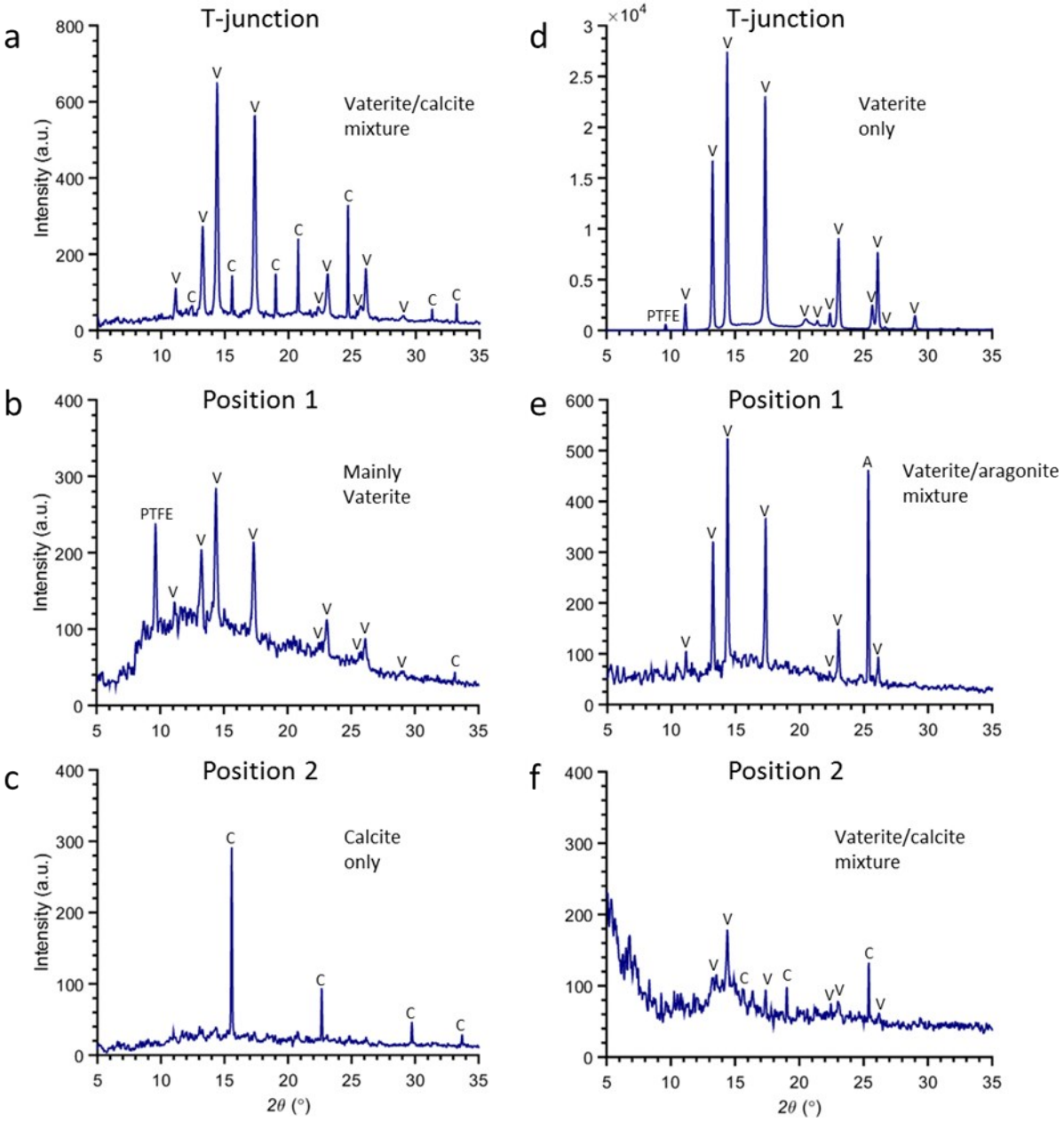

Fig. S10: (a) Thermal image of the device taken under X-ray experimental conditions (cartridge heater at ~130 °C and total flow rate of 14 µL min^{-1}). (b) Graphs of temperature vs. channel position for four flow rates (7, 14, 28, and 42 µL min^{-1}). The cartridge heater was maintained at ~130 °C. The best fit lines were determined through a cubic smoothing spline with a smoothing parameter of $p = (1 + 10 \cdot \frac{h^3}{16})^{-1}$, where h is the average distance between channel positions.

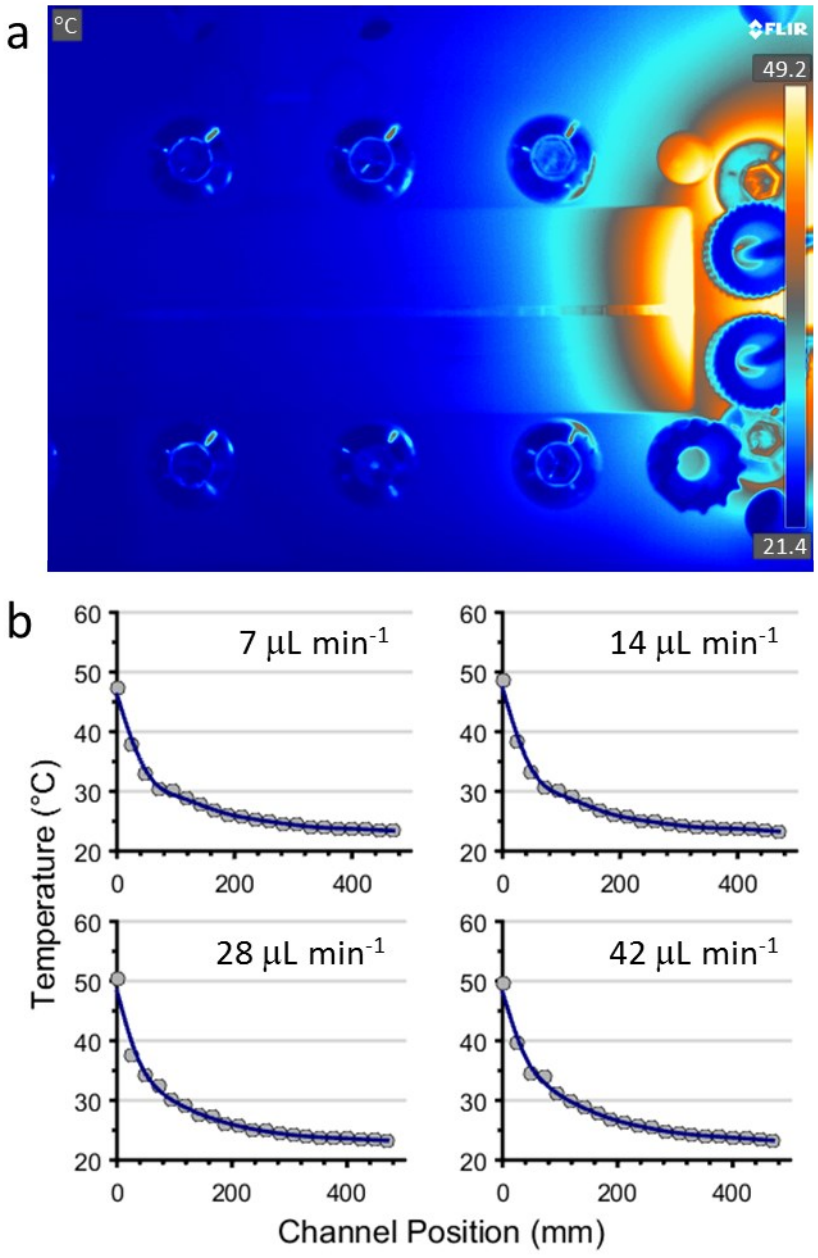

Fig. S11: Initial XRD pattern from the T-junction in the continuous flow temperature gradient experiment compared to literature references for ACC scattering. Patterns were normalized and the T-junction pattern was converted from the beamline wavelength to Cu Kα (1.5406 Å).

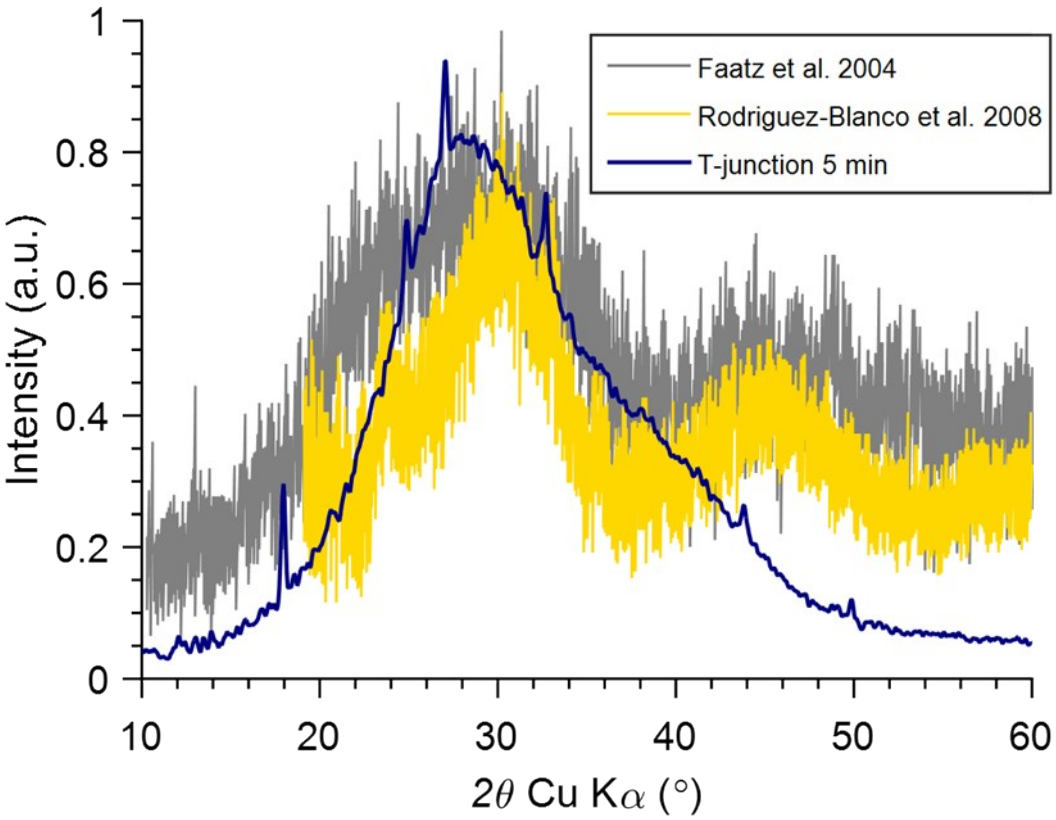

Fig. S12: (a-l) Optical micrographs taken from the temperature gradient continuous flow experiment at the indicated time and position. (m-o) Scanning electron micrographs of the bottom Kapton window revealing surface growth after running the experiment for 40 min. Scale bars are 100 μm in optical images and are 50 μm in SEM images.

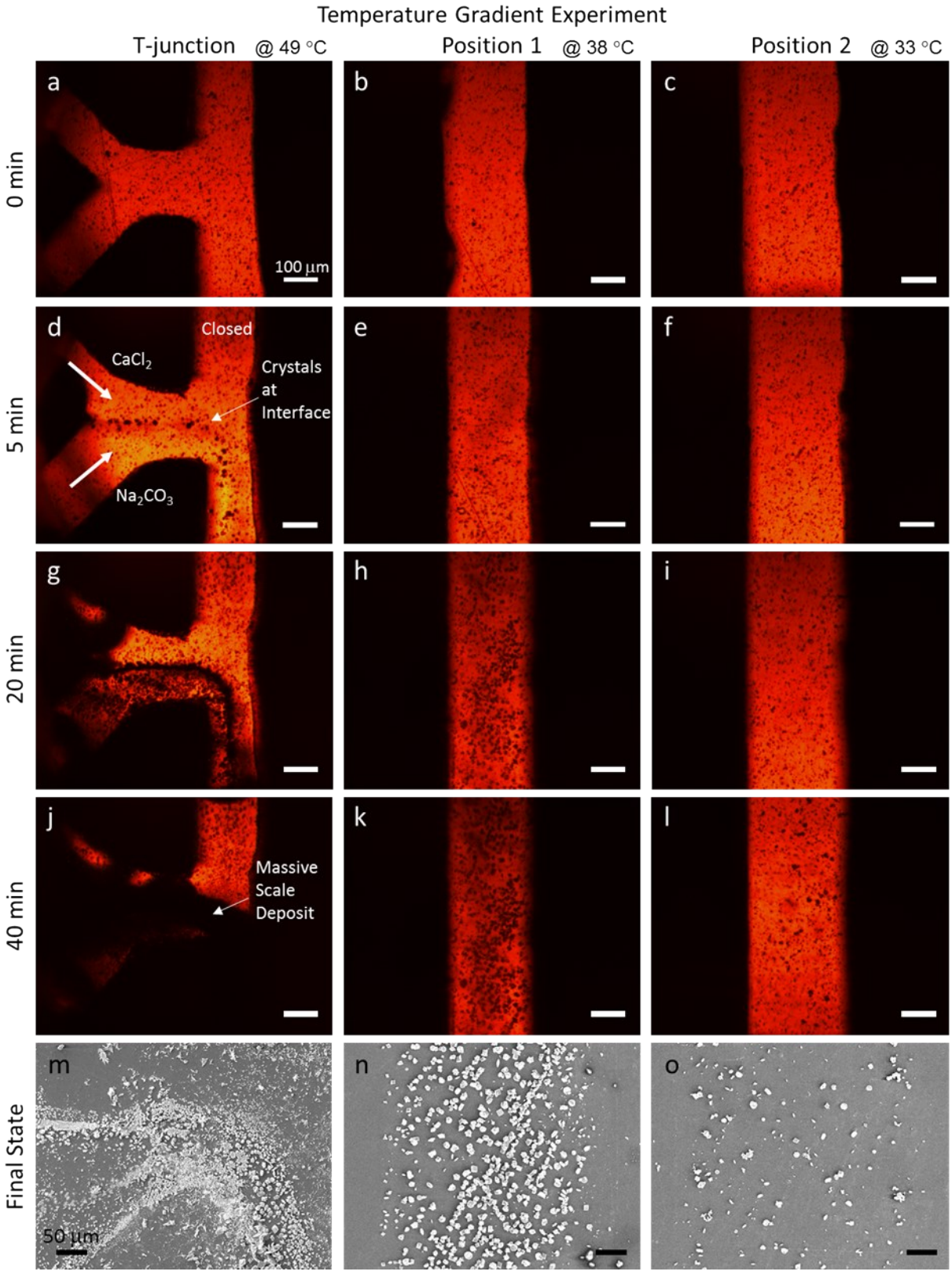

Fig. S13: Optical snapshot of droplets passing by Positions 4 and 5 after 40 min of segmented flow without a buffer channel. Solid precipitate can be seen within the droplet at Position 4.

Fig. S14: SEM micrographs of the indicated device position after the indicated experiment type. All scale bars are 50 μm.

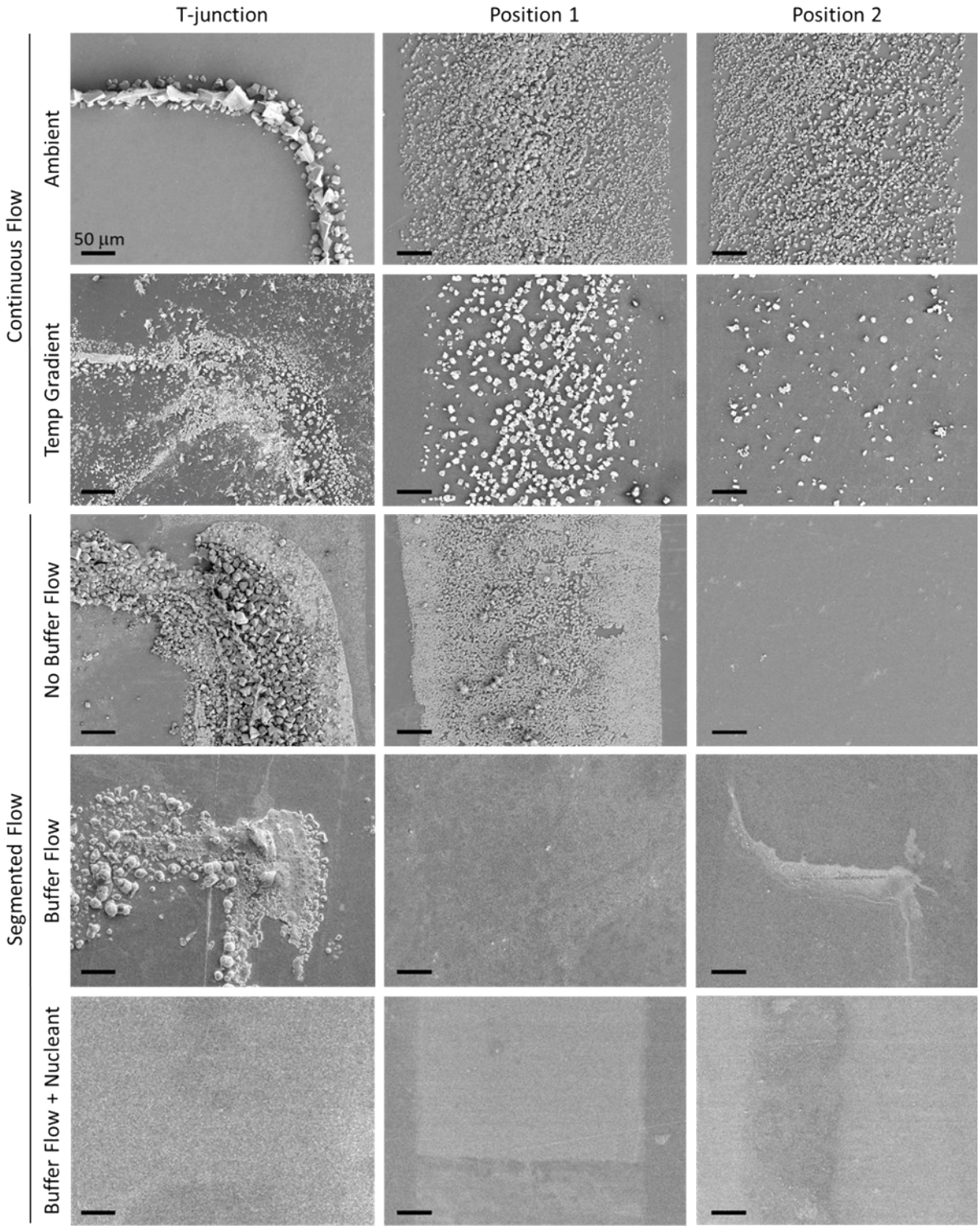

Fig. S15: (a) Time-resolved imaging of the T-junction during segmented flow experiments with a buffer flow and without a nucleating agent. The last panels display SEM micrographs of the final state of the T-junction. Scale bars in optical images are 200 μm and are 50 μm in SEM images. (b) Spatially-resolved X-ray diffraction patterns and (c) time-resolved integrated intensity plots from the segmented flow condition with buffer flow and without nucleating agent. No consistent diffraction growth pattern was observed, implying the induction time of crystal nucleation was greater than the residence time of the chip. The isolated diffraction collected is attributed to scale arising from T-junction fouling.

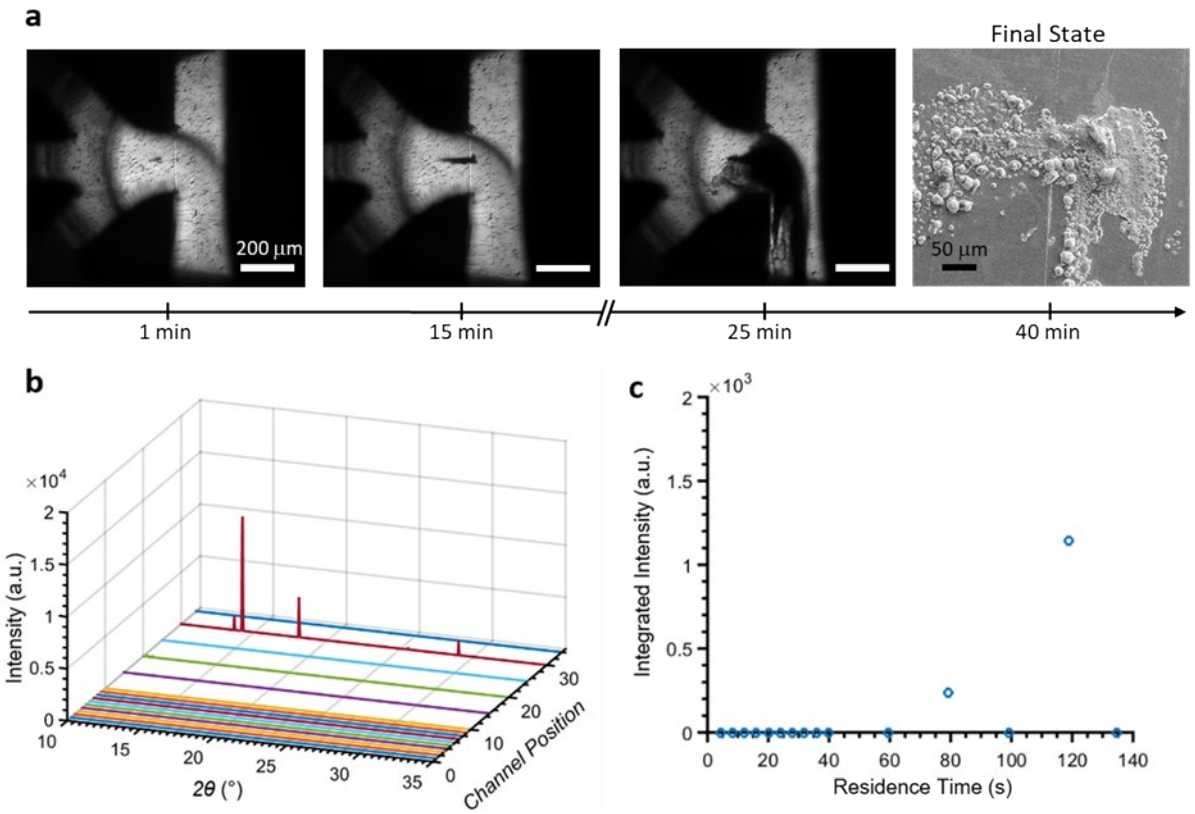

Fig. S16: Comsol simulation of the buffer flow configuration. (a) 2D slice of the Ca^{2+} concentration gradient in the centre XY plane of the aqueous inlet region of the insert-based device. The black lines refer to (1) the inlet and (2) the outlet of the nozzle leading to the T-junction. (b) Line profiles of the Ca^{2+} and CO_3^{2-} concentration gradients at (1) and (2) showing that mixing of Ca^{2+} and CO_3^{2-} ions is delayed by the central water flow. Y = 0 refers to the xyz centre of the channel, with positive Y-values closer to the CO_3^{2-} inlet and negative Y-values closer to the Ca^{2+} inlet.

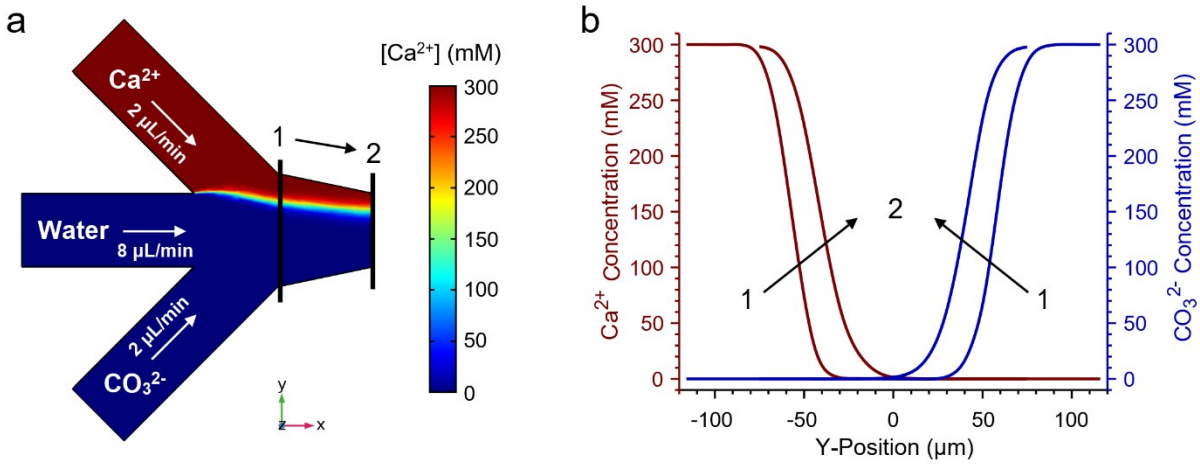

Fig. S17: 2D and 1D DMC-XRD patterns from Position 10 during a segmented experiment with buffer flow and nucleating agents after (a and b) 10 min and (c and d) 25 min experiment time. Each pattern represents data collected from 500 consecutive frames of 0.02 s exposure time each. All peaks correspond to calcite and are labelled with their corresponding lattice plane. The number and intensity of peaks in both patterns are similar. Further, image analysis of the 2D plots in Matlab revealed a similar number of connected components (discrete features in the pattern), equating to the number of individual reflections captured. In (a) there are 485 and in (b) there are 469 connected components (within 96%).

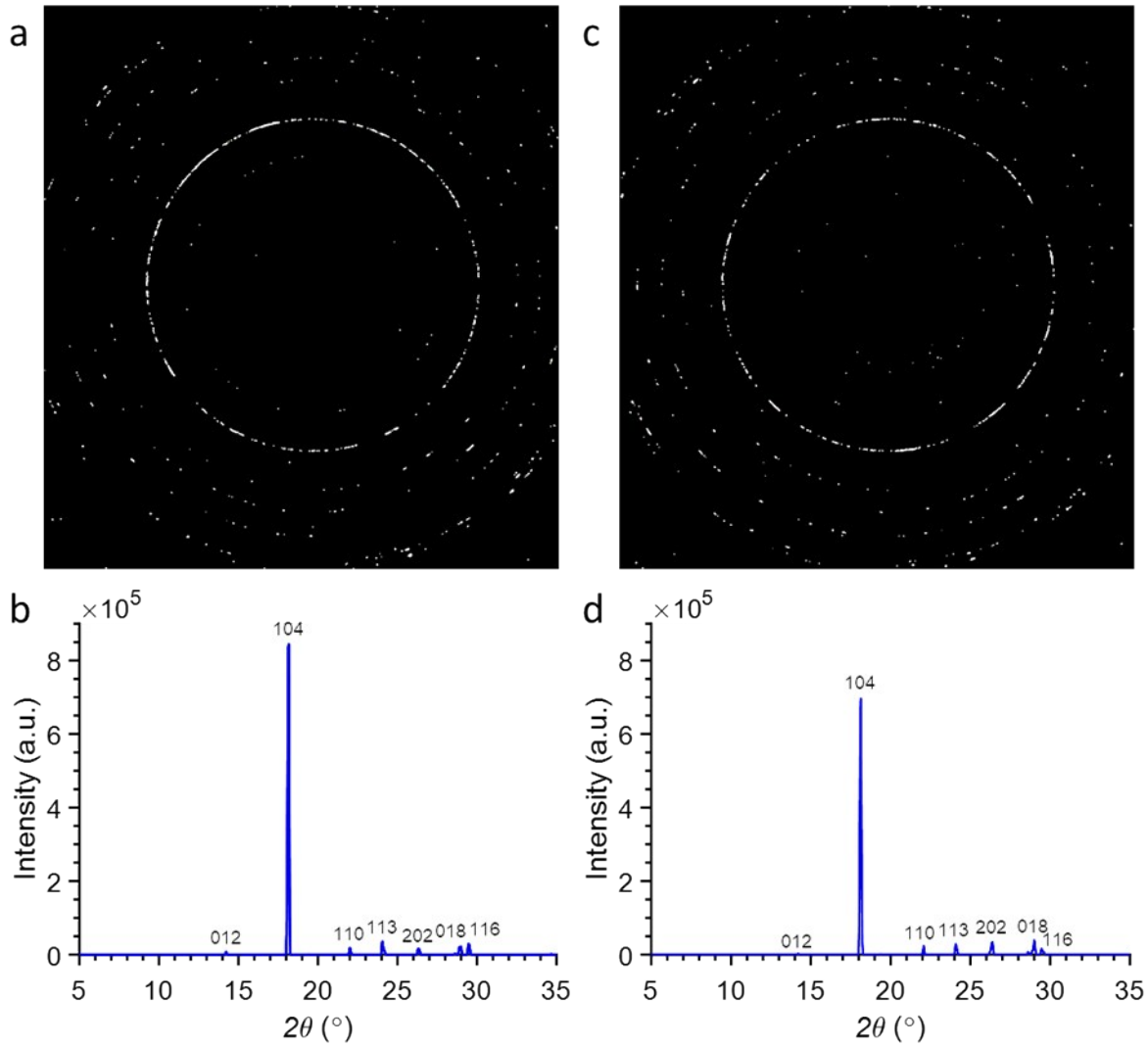

Fig. S18: Collage of 500 diffraction frames (consecutive 0.02 s exposures over 10 s) revealing the uniform ~2 Hz flow of droplets (dark frames) in FC-40 oil (light frames) in a segmented flow with buffer and nucleating agent experiment.

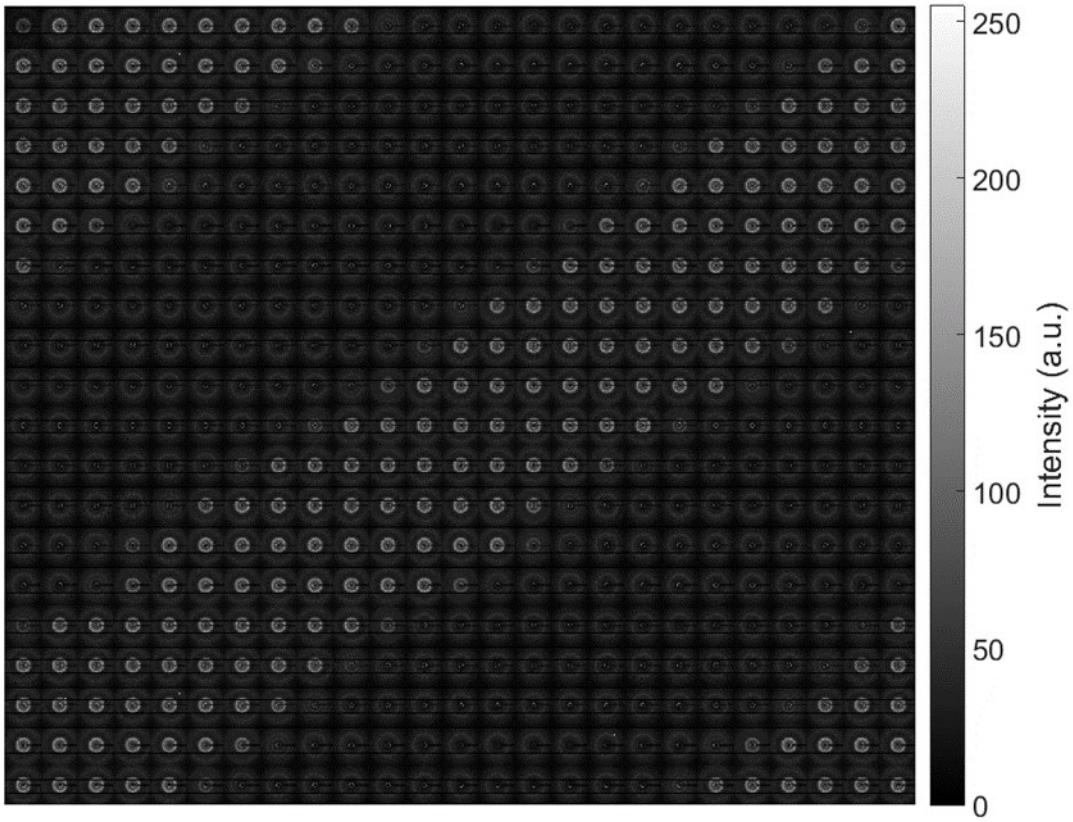

Fig. S19: (a-b) X-ray diffraction patterns obtained from 60 s exposures at Diamond I11 taken during (a) continuous flow of water and (b) segmented flow of 12.5 mM Ca^{2+} / 50 mM CO_3^{2-} aqueous droplets in FC-40 oil. The scattering from the oil dominates the diffraction pattern and no crystals can be observed. (c-d) Diffraction patterns obtained from 20 ms exposures at ESRF ID13 taken during segmented flow of 25 mM Ca^{2+} / CO_3^{2-}. (c) A frame during oil transit through the beam. (d) A frame during droplet transit, showing crystalline reflections.

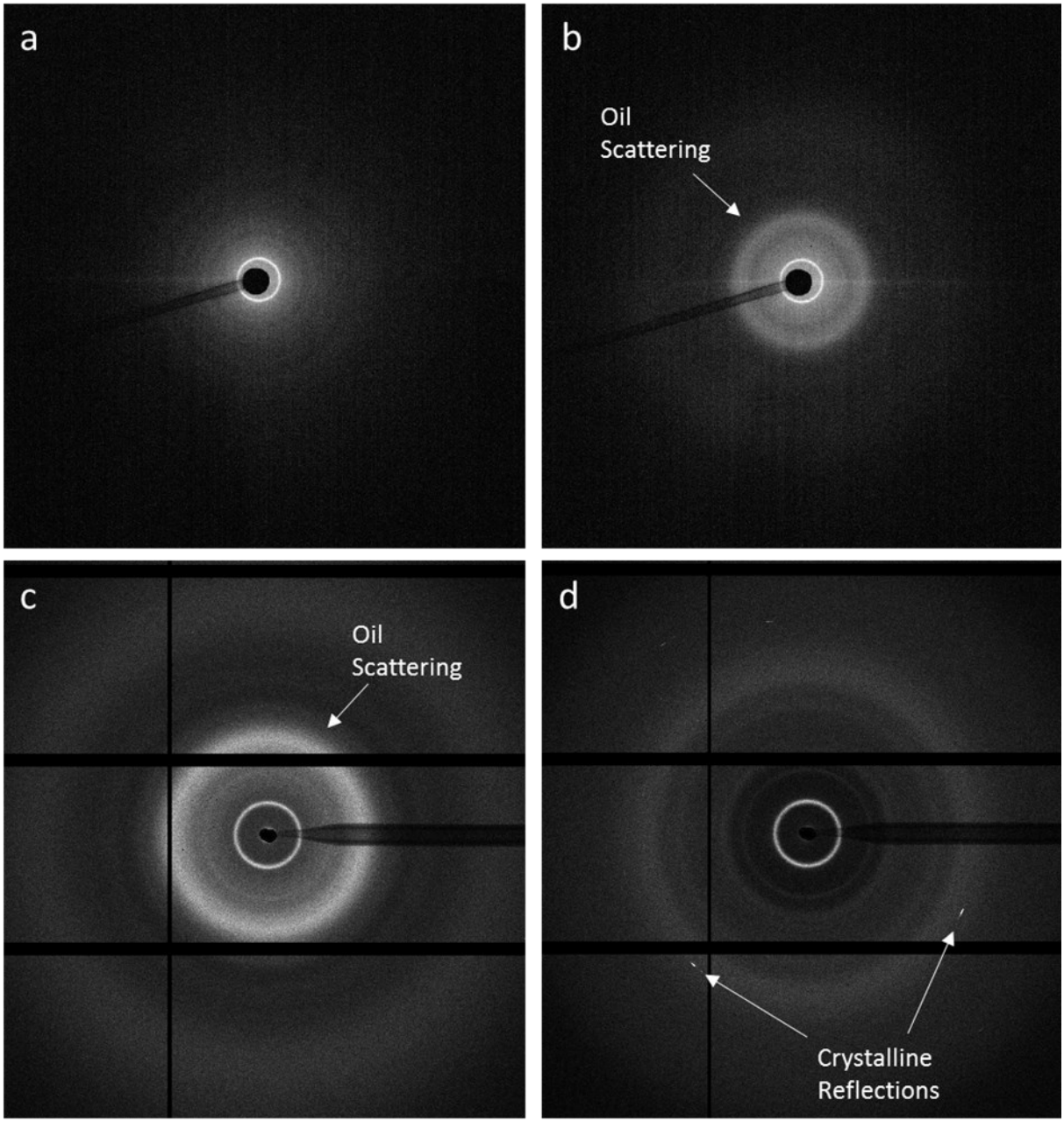

Fig. S20: Illustration of the changing quality of droplet data acquired through single frame vs. multi-frame exposures. In a single frame exposure, crystalline signal is obscured by oil scattering. However, with multi-frame data acquisition at a rate above the Nyquist frequency of droplet transit, crystalline diffraction can be isolated from oil scattering.